

Ground state correlations on ground state densities and total binding energies of ^{40}Ca , ^{48}Ca and ^{208}Pb

F. Minato¹, H. Sagawa², and S. Yoshida³

¹*Nuclear Data Center, Japan Atomic Energy Agency, Tokai, Ibaraki
319-1195, Japan*

**E-mail: minato.futoshi@jaea.go.jp*

¹*RIKEN Nishina Center, Wako, Saitama 351-0198, Japan*

²*RIKEN Nishina Center, Wako, Saitama 351-0198, Japan*

²*Center for Mathematical and Physics, the University of Aizu,
Aizu-Wakamatsu, Fukushima 965-8580, Japan*

³*Science Research Center, Hosei University, 2-17-1 Fujimi, Chiyoda, Tokyo
102-8160, Japan*

.....
 Neutron and proton densities of doubly-closed shell nuclei ^{40}Ca , ^{48}Ca and ^{208}Pb are studied based on a Hartree-Fock model with SAMi, SAMi-J27 and SAMi-T energy density functionals (EDFs). The ground state correlations (GSC) induced by isoscalar and isovector phonons are also evaluated by the second order perturbation theory with a self-consistent random phase approximation (RPA). We found that the interior part of the ground state densities is reduced by the GSC in consistent with the experimental data. On the other hand, the GSC enhances the neutron skin thickness of ^{48}Ca and ^{208}Pb . The effect of GSC on the total binding energy is also evaluated by the quasi-boson approximation. The effect of the tensor interaction is found small on both the density distributions and the binding energies.

Subject Index ground state density, binding energy, Hartree-Fock approximation, ground state correlation

1 Introduction

Mean field models have been quite successful to describe gross features of ground state mean square radii and the total binding energies of many nuclei in a wide region of the mass table [1–3]. Recent studies of the density distributions of doubly-closed shell nuclei show appreciable differences between experimental and theoretical predictions not only in the interior part but also the surface region [4, 5]. In the Hartree-Fock (HF) model for the doubly-closed shell nuclei, the single-particle orbits are fully occupied up to the Fermi energy from the bottom of the potential and no occupation probabilities of the orbits above the Fermi energy. On the other hand, it has been reported by experiments [6, 7] and theoretical large-scale shell model calculations in ^{40}Ca [8–12] that partial occupation probabilities of the orbits take values between 0 and 1, especially around the Fermi energy. These partial occupations are mostly induced by the many-body correlations beyond the mean field models.

In this paper, we study the ground state correlations (GSCs) induced by phonons calculated by a self-consistent Hartree-Fock (HF)+random phase approximation (RPA) with Skyrme energy density functionals (EDFs). The GSC are evaluated in the second-order perturbation model for the ground state densities, and the quasi-boson approximation for the total binding energies of ^{40}Ca , ^{48}Ca and ^{208}Pb . A similar study has been performed in Ref. [13, 14] for ^{16}O , $^{40,48}\text{Ca}$, and ^{208}Pb . This work, however, studies the GSC with a modern version of Skyrme parameters, SAMi [15], SAMi-J27 [16], and SAMi-T [17] EDFs and also focuses on the effect of the tensor force.

The paper is organized as follows. Section II is devoted to describe the theoretical model for GSC. Numerical results are given in Section III. Summary and future perspectives are given in Section IV.

2 Model for GSC

The ground state density distributions of doubly-closed shell nuclei are commonly calculated by the Skyrme Hartree-Fock (SHF) model assuming spherical symmetry. The density distribution of radial component is given as

$$\rho_q(r) = \sum_{k=m,i} n_k \frac{2j_k + 1}{4\pi} |\varphi_k(r)|^2 \quad (q = p, n), \quad (1)$$

where n_k , φ_k and j_k are the occupation probability, the single-particle wave function of radial part and the total angular momentum for state k , respectively. Here, we denote m for particle states and i for hole states. The occupation probabilities are $n_m = 0$ and $n_i = 1$ for

the HF density distribution. In case of the perturbed density distribution, the occupation probabilities are modified within the number-operator method [18] to be

$$\begin{aligned} n_m &= \frac{1}{2(2j_m + 1)} \sum_{i\lambda J^\pi} (2J + 1) |Y_{mi}(\lambda J^\pi)|^2 \\ n_i &= 1 - \frac{1}{2(2j_i + 1)} \sum_{m\lambda J^\pi} (2J + 1) |Y_{mi}(\lambda J^\pi)|^2. \end{aligned} \quad (2)$$

where $Y_{mi}(\lambda J^\pi)$ is the backward amplitude of the phonon operator of random phase approximation. The label λ and J^π represent the λ -th excited RPA phonon state and its spin-parity, respectively. The RPA phonon creation operator is defined as

$$Q^\dagger(\lambda J^\pi) = \sum_{mi} X_{mi}(\lambda J^\pi) a_m^\dagger a_i - Y_{mi}(\lambda J^\pi) a_i^\dagger a_m. \quad (3)$$

The coefficients of $X_{mi}(\lambda J^\pi)$ and $Y_{mi}(\lambda J^\pi)$ are determined by solving the RPA equation [19].

The rms radii are calculated by

$$r_q \equiv \sqrt{\langle r^2 \rangle_q} = \sqrt{\frac{1}{N_q} 4\pi \int \rho_q(r) r^4 dr}, \quad (4)$$

where $N_p = Z$ and $N_n = N$. The neutron skin thickness is estimated by $\Delta r_{np} = r_n - r_p$.

To calculate the unperturbed and perturbed density distributions numerically, we adopt the SHF model in the coordinate space. To solve the RPA equation, we take into account the single particle states up to 60 MeV in energy, and restrict unperturbed $1p$ - $1h$ excitations energy up to 100 MeV in the model. The continuum states are discretized by a finite box with a size of $R = 20$ fm. We consider the spin-parity states up to $J^\pi = 5^\pm$. We confirm that the model space is enough to make the calculated occupation probabilities of Eq. (2) converge. The residual interactions, the second-derivative of SHF EDF with respect to densities, are self-consistently taken into account in the RPA except for spin-orbit component, which is however not significant. Within this model space, the energy-weighted sum rules are satisfied over 99.5% for all J^π .

3 Results

3.1 Density distributions and rms radii

Table 1 shows nuclear proton and neutron rms radii of ^{40}Ca , ^{48}Ca and ^{208}Pb calculated by using a modern version of Skyrme parameters, SAMi, SAMi-J27, and SAMi-T EDFs. Both the results of HF and HF+GSC calculations are listed and compared with experimental data. The tensor interactions are included in SAMi-T EDF. The proton radii or

Table 1 Proton and neutron rms radii of ^{40}Ca , ^{48}Ca , and ^{208}Pb . The neutron skin is given as $\Delta r_{np} \equiv r_n - r_p$. HF denotes the results of HF calculations, while HF+GSC includes also the ground state correlations. The experimental data are taken from [4] for ^{40}Ca , ^{48}Ca and from [5] for ^{208}Pb . The experimental errors of Δr_{np} include both statistical errors and model uncertainties. The radii are given in unit of fm.

Nuclei		SAMi		SAMi-J27		SAMi-T		exp.
		HF	HF+GSC	HF	HF+GSC	HF	HF+GSC	
^{40}Ca	r_n	3.343	3.773	3.344	3.810	3.339	3.808	3.375
	r_p	3.390	3.853	3.391	3.870	3.386	3.845	3.385
	Δr_{np}	-0.047	-0.080	-0.047	-0.060	-0.046	-0.037	$-0.010^{+0.049}_{-0.048}$
^{48}Ca	r_n	3.612	4.003	3.588	4.006	3.589	4.004	3.555
	r_p	3.436	3.770	3.444	3.801	3.424	3.781	3.387
	Δr_{np}	0.176	0.233	0.144	0.205	0.166	0.223	$0.168^{+0.052}_{-0.055}$
^{208}Pb	r_n	5.610	5.750	5.580	5.731	5.574	5.730	5.653
	r_p	5.463	5.555	5.456	5.553	5.421	5.517	5.442
	Δr_{np}	0.147	0.195	0.123	0.178	0.153	0.213	$0.211^{+0.054}_{-0.063}$

equivalently the charge radii of ^{40}Ca and ^{208}Pb are in general included in the optimized data set. Therefore it is not a surprise that HF results reproduce well the proton radii of these nuclei. The neutron radii of ^{40}Ca and ^{208}Pb are slightly smaller than the experimental ones. Including the GSC, the neutron skin of ^{208}Pb increases and becomes closer to the experimental value compared with the HF result. On the other hand, the neutron skin of ^{40}Ca becomes a larger negative value with the GSC in the cases of SAMi and SAMi-J27, while SAMi-T with the tensor term gives slightly better agreement with the experimental value $\Delta r_{np} = -0.01$ fm. In ^{48}Ca , all the three HF results in Table 1 give slightly larger radii than the experimental one for both protons and neutrons, while the neutron skin is well reproduced by the HF calculations, especially in the case of SAMi-T. The GSC enlarges both the proton and the neutron radii and the quantitative agreement becomes worse than HF results by about 0.4 fm. Experimental data of the neutron skin of ^{208}Pb is still controversial. The dipole polarizability experiment gives $\Delta r_{np} = 0.156^{+0.025}_{-0.021}$ fm [21], while the parity violation electron scattering experiment PREXII were analyzed by two different models and the neutron skin was extracted to be $\Delta r_{np} = 0.283 \pm 0.071$ fm [22] and $\Delta r_{np} = 0.19 \pm 0.02$ fm [23], respectively. The present calculations, both HF and HF+GSC, are unlikely to reproduce the experimental data of PREXII reported in ref. [22].

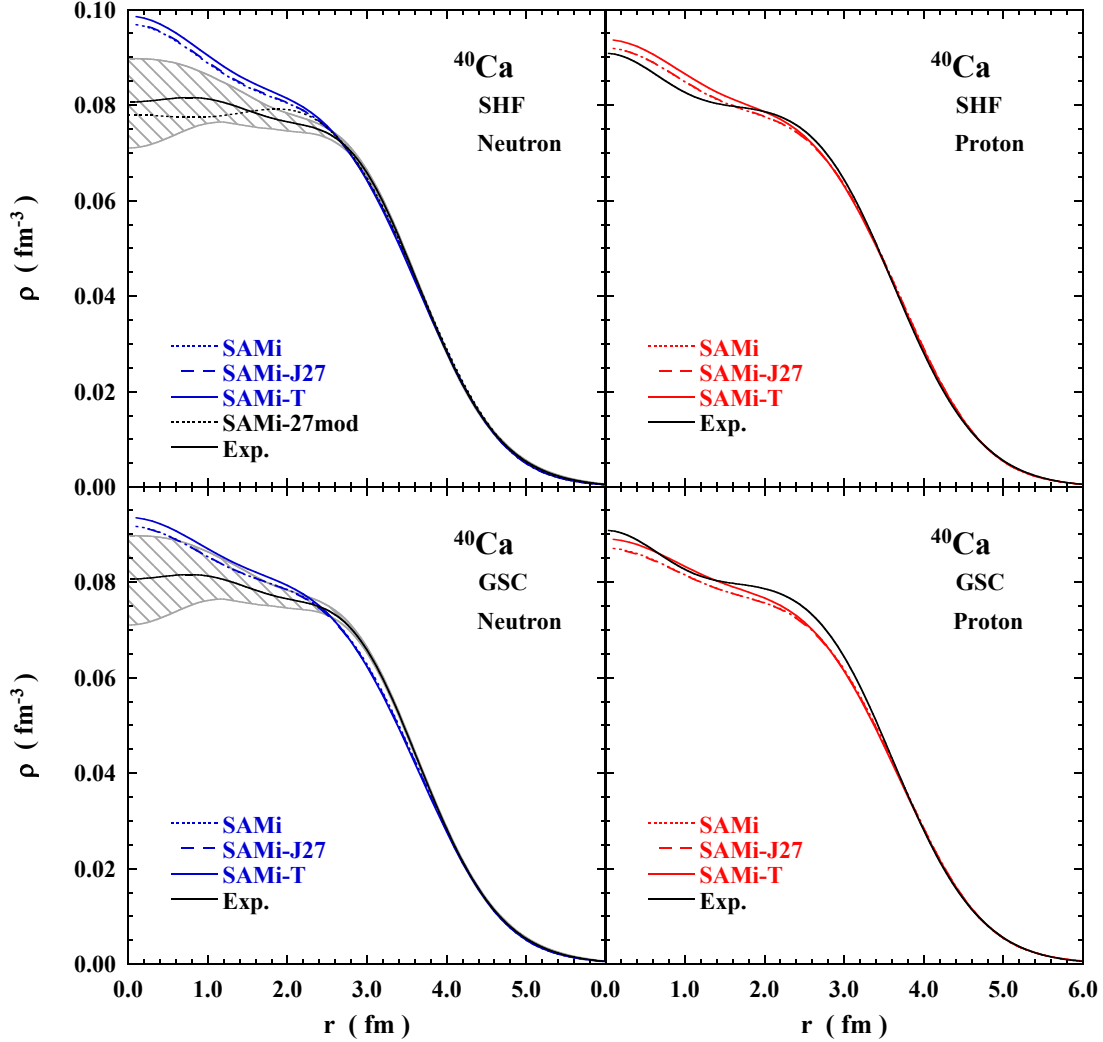


Fig. 1 (color online) Neutron (left panels) and proton (right panels) density distributions of ^{40}Ca . Upper panels show the HF results with three SAMi EDFs, SAMi, SAMi-J27 and SAMi-T, respectively. The SAMi-T has the tensor terms, while the SAMi and SAMi-J27 have no tensor terms. The black solid lines show experimental data taken from Ref. [24] for protons and from Ref. [4] for neutrons. The shaded area of experimental neutron density shows experimental uncertainties of both statistical and systematic errors. The neutron density distribution denoted SAMi-J27mod in the upper left panel is obtained by optimizing the occupation probabilities of neutrons as given in Table 2.

Figure 1 shows comparisons between calculated and experimental neutron (left panel) and proton (right panel) densities of ^{40}Ca . Upper panels show the HF results, and the lower panels correspond to the results of HF+GSC. The HF densities of both neutrons and protons

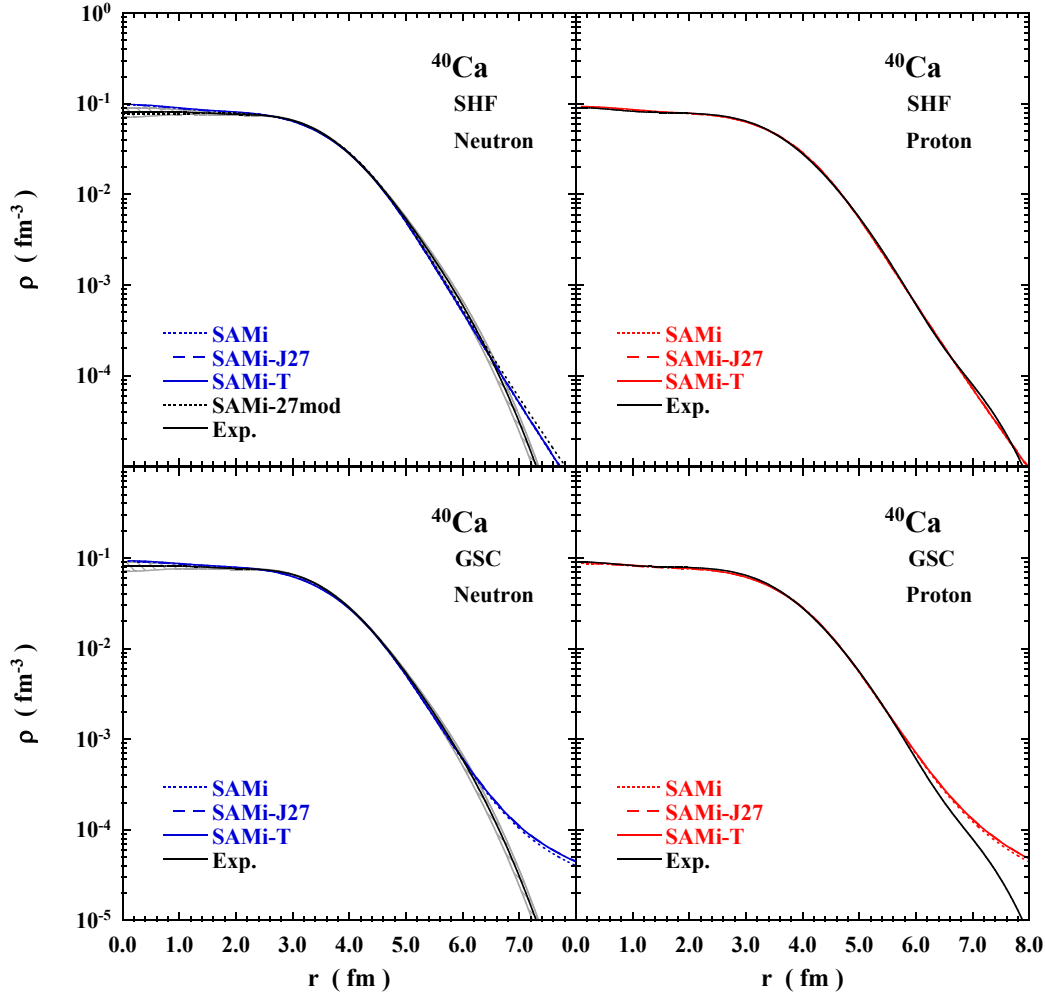


Fig. 2 (color online) Neutron and proton density distributions of ^{40}Ca in the log scale. The upper panels show the HF results, while the lower panels are the HF+GCS results. Experimental data are shown by a black solid curve. The model dependence of EDFs is not visible in this scale.

somewhat overestimate in the interior part. The EDF model dependence is rather small: the SAMi and SAMi-J27 give almost identical results for the density distributions, while SAMi-T enhances the interior region of density more than other two interactions. On the contrary, the calculated results slightly underestimate the shoulder part at around 3 fm. With the GSC, the central part is hindered and become closer to the experimental density distribution, especially in the case of proton density. On top of that, the shoulder part is also quenched and small amount of density is shifted to $r > 6$ fm region. In the upper left panel of Fig. 1, the

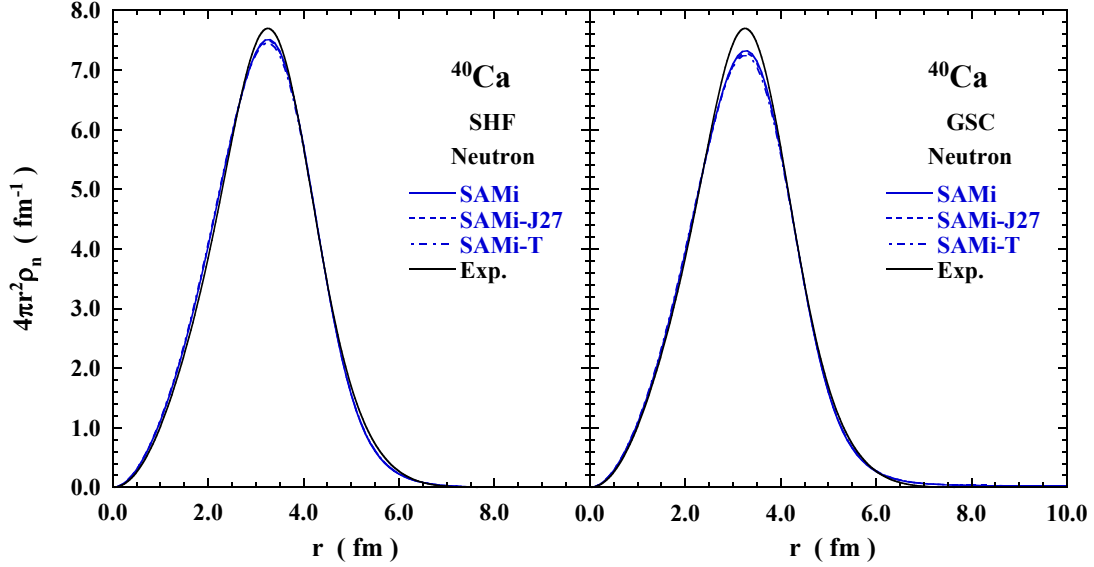


Fig. 3 (color online) Neutron density distributions of ^{40}Ca with a factor of $4\pi r^2$. The left panel shows the HF results, while the right panel are the HF+GCS results. Experimental data are shown by a black solid curve. The model dependence of EDFs is not visible in this scale.

neutron density distribution denoted SAMi-J27mod is shown by optimizing the occupation probabilities of neutrons as given in Table 2 in order to reproduce the experimental density. The difference between HF and HF+GSC at $r > 6.5$ fm is clearly seen in Fig. 2 where the densities are plotted in log scale. In this scale, the interaction dependence does not appear in the entire region of coordinate space.

Figure 3 shows the neutron density distribution of ^{40}Ca without and with GSC multiplied by a factor $4\pi r^2$. The differences between HF and HF+GSC appear in the central region $r < 2$ fm, the peak height at $r = 3.2$ fm, in the tail region $5 \text{ fm} < r < 6 \text{ fm}$, and also at the very low density region $r > 6.5$ fm. We can see small improvements of agreements by GSC at the central region and also at the surface. On the other hand, the peak height is quenched by GSC and a small amount of density is pushed to outside of the surface region in contrast to the experimental data.

Figure 4 shows comparisons between calculated and experimental densities of neutrons (left panel) and protons (right panel) of ^{48}Ca . The essential features are the same as those of ^{40}Ca . One peculiar difference is the shoulder peak of neutron density due to the $f_{7/2}$ neutron occupation in ^{48}Ca . The HF densities of both neutrons and protons slightly overestimate in the interior part. The EDF model dependence is again rather small for ^{48}Ca . The calculated

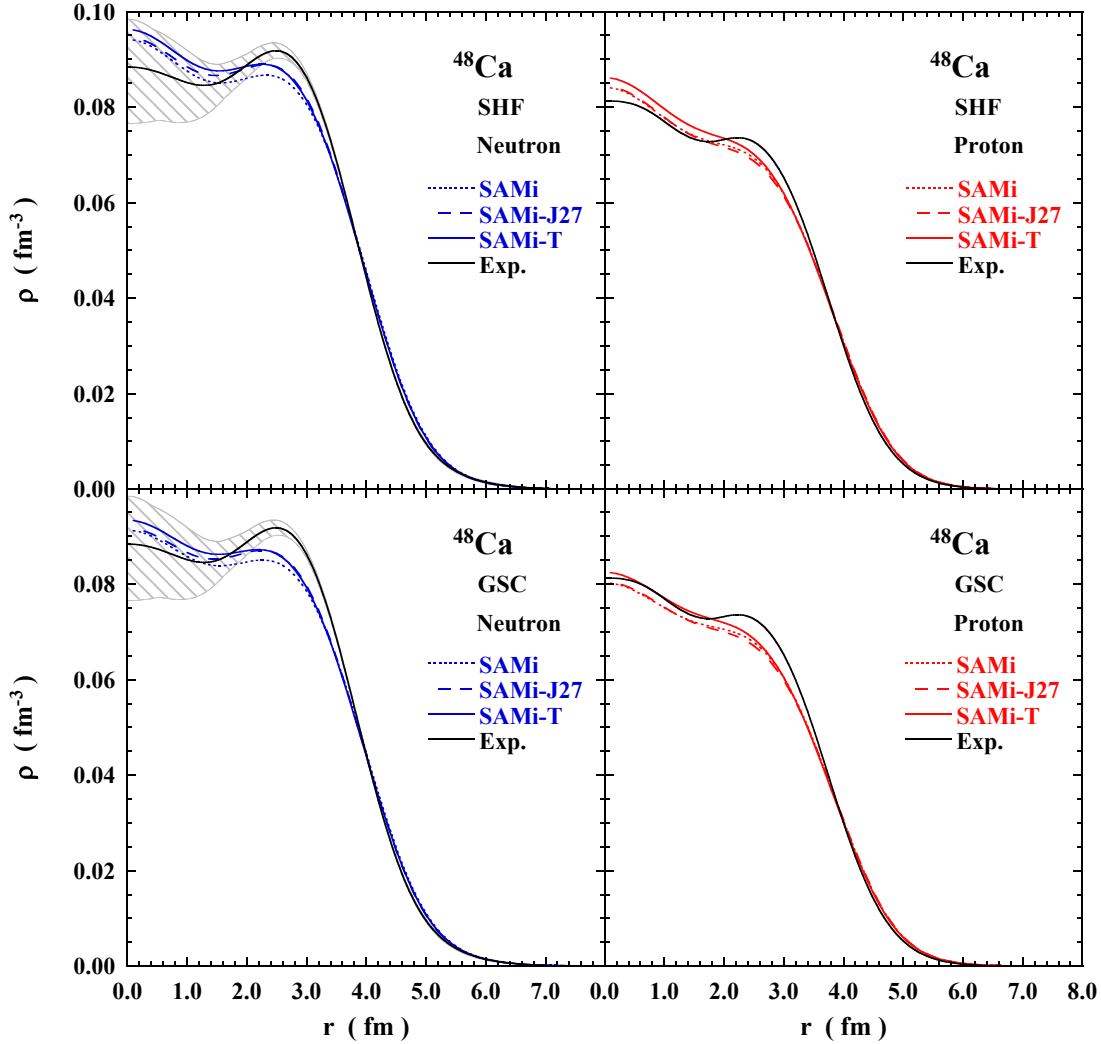


Fig. 4 (color online) The same as Fig. 1, but for ^{48}Ca .

results underestimate the shoulder part at around 3 fm. With the GSC, the central part is hindered and become closer to the experimental density distribution, or even underestimate in the case of proton density. The shoulder part is also quenched and small amount of density is shifted to $r > 6$ fm region. The densities of ^{208}Pb are shown in Fig. 5. For the proton density (right panel), the HF results reproduce well the plateau between $r = 2.0$ fm and $r = 5.5$ fm, while they show larger values at the central part at $r < 1.5$ fm than the experimental data. The GSC effect on the proton density of ^{208}Pb is relatively small even compared with ^{40}Ca and ^{48}Ca . Nevertheless, we can see that the HF+GSC improves slightly the agreement at the interior part of proton density at the right panels of Fig. 5. For the neutron density, the

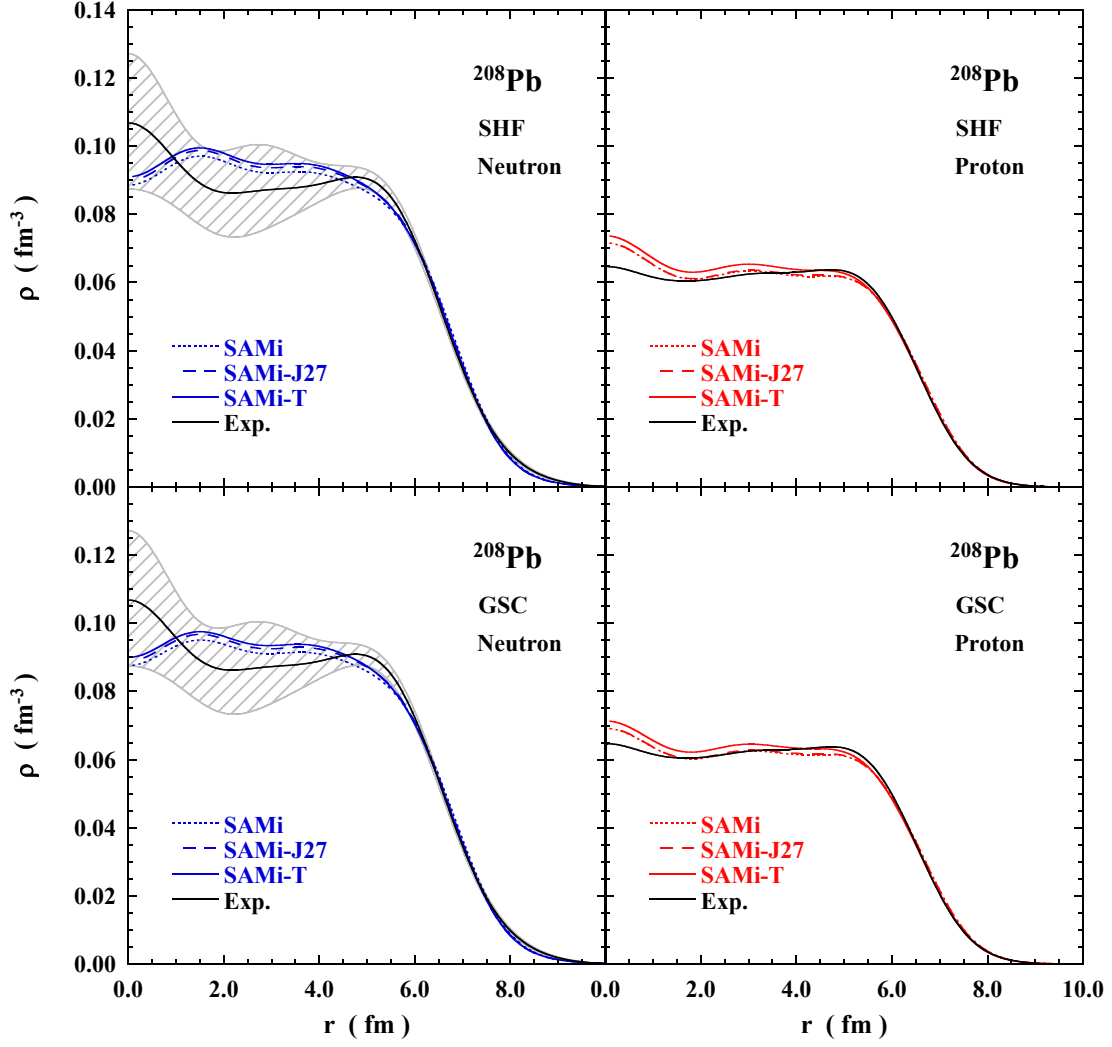


Fig. 5 (color online) The same as Fig. 1, but for ^{208}Pb . Experimental data taken from Ref. [24] for protons and from Ref. [5] for neutrons.

HF results give slightly larger density for the plateau between $r = 1.0$ and $r = 5.5$ fm, while underestimate the central part $r < 1$ fm. These disagreements are somewhat improved in the case of HF+GSC results and the calculated results are within the experimental uncertainties at $r < 5$ fm. The density distribution at $r > 8$ fm becomes larger than that of HF similar to the case of ^{40}Ca shown in Fig. 2.

3.2 Particle occupation numbers of *sd*-shell and *pf*-shell orbits in ^{40}Ca

In Table 2, the occupation probabilities of various calculations are listed with the empirical proton and neutron occupation probabilities in ^{40}Ca . Skyrme HF-Bogolyubov calculations are performed with SAMi interaction and the volume-type and mixed-type pairing interactions with the code HFBTHO [12]. We found that there are essentially no occupation probabilities v_j^2 in *pf*-shell orbits because of a large shell gap between $1d_{3/2}$ and $1f_{7/2}$ orbits. The GSCs with SAMi and SAMi-T give small amounts of the occupation probabilities in the *pf*-shell orbits, $\sum_{pf}(2j+1)v_j^2 \approx 0.3$. There is no essential difference between SAMi and SAMi-T without and with the tensor terms.

The results of several Large Scale Shell Model (LSSM) calculations are also listed in Table 2, which depend largely on the model space and the adopted interactions. In Refs. [8, 10, 11], LSSM calculations have been performed including many-particle many-hole excitations from *sd*-shell to *pf*-shell configurations. In Ref. [8], the active model space is $(1d_{3/2}, 1f_{7/2}, 2p_{3/2})$, while the $1d_{3/2}, 2s_{1/2}$ orbits are also included in Ref. [10]. Shell model calculations with the configurations of 2-particle 2-hole (2p-2h) and 4p-4h excitations from the closed shell core of ^{40}Ca are also performed in Ref. [11]. The full *sd* and *pf* shell orbits are involved with *sdpf*-mu shell model effective interactions. The occupation probabilities of *1f*-orbits go up to $\sum_f(2j+1)v_j^2 \approx 0.6$, but those of *p*-shell orbits are rather small as less than 0.1. The empirical occupation numbers are also listed obtained from proton transfer reactions [6], and also from the analysis of neutron density distributions denoted as SAMi-J27mod in Fig. 1 [12]. The proton transfer data suggest the same amount of the proton occupation probabilities in *pf*-shell orbits as the shell model predictions. On the other hand, the experimental neutron density distribution requires the occupation probability of *f*-orbits to be ~ 1.2 , which is two times larger than the proton transfer experiments.

3.3 Correlation energies for the total binding energies

The correlation energies due to the ground state correlations are calculated within the framework of RPA and quasi-boson approximation [18]:

$$E_{\text{corr}} = \sum_{\lambda J \pi} (2J+1) E(\lambda J \pi) \sum_{mi} |Y_{mi}(\lambda J \pi)|^2. \quad (5)$$

The sum of phonon states λ in Eq. (5) is restricted to those absorb a fraction of the non-energy-weighted sum rule larger than 1% for isoscalar or isovector transition strength. The results are tabulated in Table 3. As is expected, the HF calculations give already reasonable agreement with the experimental total binding energies since all the parameters are optimized

Table 2 Particle occupation numbers, $(2j + 1)v_j^2$, for neutron sd -shell and pf -shell configurations of ^{40}Ca . The column with a bar (—) is not involved in the shell model calculations or analysis of experimental data. Experimental data of proton transfer reaction are taken from Ref. [6].

Model	$1s_{1/2}$	$2p_{3/2}$	$2p_{1/2}$	$1d_{5/2}$	$2s_{1/2}$	$1d_{3/2}$	$1f_{7/2}$	$2p_{3/2}$	$2p_{1/2}$	$1f_{5/2}$
HFB (SAMi)	2.00	4.00	2.00	6.00	2.00	4.00	0.00	0.00	0.00	0.00
HF+GSC(SAMi)	1.964	3.908	1.949	5.761	1.843	3.792	0.206	0.049	0.010	0.040
HF+GSC(SAMi-T)	1.968	3.905	1.954	5.753	1.845	3.776	0.201	0.052	0.009	0.076
GSC (RPA) [20]	1.92	3.76	1.88	5.58	1.8	3.7	0.24	0.16	0.08	—
d pf -shell [8]	—	—	—	—	—	3.30	0.63	0.07	—	—
$sdpf$ -msd4 [10]	—	—	—	5.902	1.908	3.477	0.617	0.096	—	—
$sdpf$ -mu ($2p$ - $2h$) [11]	—	—	—	5.864	1.933	3.845	0.191	0.040	0.020	0.107
$sdpf$ -mu ($4p$ - $4h$) [11]	—	—	—	5.727	1.854	3.660	0.421	0.089	0.041	0.208
exp. (p-transfer) [6]	—	—	—	6.0	1.70	3.59	0.56	0.15		
SAMi-J27mod [12]	2.00	4.00	2.00	6.00	1.342	3.431	1.227			

Table 3 The HF total binding energies and correlation energies due the ground state correlations of $^{40,48}\text{Ca}$ and ^{208}Pb . The experimental data are taken from AME2020 [25]. The correlation energies are calculated by using Eq. (5). The value is given by a unit of MeV.

Nuclei	SAMi		SAMi-J27		SAMi-T		exp.
	E_{tot}	E_{corr}	E_{tot}	E_{corr}	E_{tot}	E_{corr}	
^{40}Ca	347.02	4.25	344.39	4.10	343.68	4.78	342.05
^{48}Ca	415.46	4.93	415.45	5.89	416.73	4.76	416.00
^{208}Pb	1635.86	3.95	1635.54	3.05	1635.39	3.41	1636.43

to reproduce a set of experimental data in which the total binding energies of the doubly-closed shell nuclei are included. The correlation energies give about 1% additional energies to the binding energies of ^{40}Ca and ^{48}Ca , while it is much smaller in ^{208}Pb to be about 0.2%. As seen in the table, the correlation energies do not give further improvement. For this reason, together with the rms radii, one needs to readjust the Skyrme parameters including the correlation effects for the consistent description of the ground state properties in the beyond mean field model.

4 Summary and future perspectives

We studied the effects of GSC on the densities and the total binding energies of doubly-closed shell nuclei ^{40}Ca , ^{48}Ca , and ^{208}Pb with modern Skyrme EDFs, SAMi, SAMi-J27 and SAMi-T. For the ground state densities, the GSC reduces slightly in the interior part of HF densities of both neutrons and protons, and gives consistent results in comparisons with the experimental data of ^{40}Ca and ^{48}Ca . The GSC decreases also the shoulder part of density at around $r = 3$ fm, and removes a small amount of density to the region $r > 6$ fm. The GSC effect is smaller in ^{208}Pb and quantitatively the same as ^{40}Ca , and ^{48}Ca .

The GSC on the total binding energy is also discussed within the quasi-boson approximation, and found to increase about 1% for $^{40,48}\text{Ca}$ and 0.2% for ^{208}Pb of the total binding energy. In order to describe these ground state observables with beyond mean field models, we need to refit Skyrme EDFs including the GSC effects for the consistent descriptions.

Acknowledgement

FM and HS thank YIPQS long-term workshop “Mean-field and Cluster Dynamics in Nuclear Systems 2022 (MCD2022)” May 9 – June 17, 2022 held at Yukawa Institute, Kyoto University, where the collaboration was started. We thank J. Zenihiro and T. Uesaka for providing the experimental data. We thank also T. Naito for useful discussions on the HF calculations. This work is supported by JSPS KAKENHI Grant Number JP19K03858. JSPS.

References

- [1] S. Goriely, N. Chamel, and J.M. Pearson, *Phys. Rev. C* 93, 034337 (2016).
- [2] Min Shi, Zhong-Ming Niu, and Hao-Zhao Liang, *Chin. Phys. C* 43, 074104 (2019).
- [3] M. Kortelainen, J. McDonnell, W. Nazarewicz, E. Olsen, P.-G. Reinhard, J. Sarich, N. Schunck, S.M. Wild, D. Davesne, J. Erler, and A. Pastore, *Phys. Rev. C* 89, 054314 (2014).
- [4] J. Zenihiro, T. Uesaka, S. Yoshida and H. Sagawa, *Prog. Theo. Exp. Phys.* 2021, 023D05 (2021)
J. Zenihiro et al., arXiv:1810.11796 (2018).
- [5] J. Zenihiro *et al.*, *Phys. Rev. C* 82, 044611 (2010).
- [6] P. Doll, G.J. Wagner, K.T. Knöpfle and G. Mairle, *Nucl. Phys. A* 263, 210 (1976).
- [7] F. Malaguti, A. Uguzzoni, E. Verondini and P. E. Hodgson, *Nucl. Phys. A* 297, 287 (1978); *ibid.*, *Nuovo Cim. A* 49, 412 (1979).
- [8] B. A. Brown, S. E. Massen, and P. E. Hodgson, *J. Phys. G: Nucl. Phys.* 5, 1655 (1979).
- [9] J. Streets, B.A. Brown and P.E. Hodgson, *J. Phys. G: Nucl. Phys.* 8, 839 (1982).
- [10] N. Shimizu, Y. Utsuno, T. Ichikawa et al., private communications (2022).
- [11] Toshio Suzuki, private communications (2022).
- [12] H. Sagawa, S. Yoshida, T. Naito, T. Uesaka, J. Zenihiro, J. Tanaka, *Physics Letters B* 829 137072 (2022).
- [13] A. Faessler, S. Krewald, A. Plastino, and J. Speth, *Z. Physik A* 276, 91 (1976).
- [14] M. Waroquier, J. Bloch, G. Wenes, and K. Heyde, *Phys. Rev. C* 28, 1791 (1983).
- [15] X. Roca-Maza, G. Colò, and H. Sagawa, *Phys. Rev. C* 86, 031306(R) (2012).
- [16] X. Roca-Maza, M. Brenna, B. K. Agrawal, P. F. Bortignon, G. Colò, Li-Gang Cao, N. Paar, and D. Vretenar, *Phys. Rev. C* 87, 034301 (2013).
- [17] S. Shen, G. Colò, and X. Roca-Maza, *Phys. Rev. C* 99, 034322 (2019).
- [18] D.J. Rowe, *Phys. Rev.* 175, 1283 (1968).
- [19] P. Ring and P. Schuck, *The Nuclear Many-Body Problem*, Springer-Verlag, New York, 1980.

- [20] H. Lenske and J. Wambach, Phys. Lett. B 249, 377 (1990).
- [21] A. Tamii et al., Phys. Rev. Lett. 107, 062502 (2011).
- [22] D. Adhikari et al. (PREX Collaboration), Phys. Rev. Lett. 126, 172502 (2021).
- [23] P.-G. Reinhard, X. Roca-Maza, and W. Nazarewicz Phys. Rev. Lett. 127, 232501 (2021).
- [24] H. de Vries, C. W. de Jager, and C. de Vries, At. Data Nucl. Data Tables **36**, 495 (1987).
- [25] W. J. Huang, M. Wang, F.G. Kondev, G. Audi, and S. Naimi, Chin. Phys. C45, 030002 (2021); Chin. Phys. C45, 030003 (2021).